# Numerical Simulation of Laser Ablation with Cavity Reflections

A. W. Bailey* and A. Modak†
*Physical Sciences, Inc., Andover, Massachusetts*

**A self-consistent ablation, heat-conduction, and radiation-transport model is required to model laser ablation of reflective targets properly. In laser-ablation experiments on metal-loaded carbon targets, the shiny metallic crater formed by the beam can act as a focusing cavity. This phenomenon results in highly augmented ablation rates in small-spot laser tests in which the aspect ratio of the cavity (depth/spot diameter) is large. The ablation and illumination processes become strongly coupled, the shape of the crater formed affecting the power distribution over the surface and therefore the ablation rate, which, in turn, determines the evolution of the crater shape. The process can be accurately described by coupling ray-tracing techniques to ablation and heat-conduction modeling. Simulations of actual experiments using this model indicate that an overestimate of up to 30% in prediction of the time required to burn through a target could result from ignoring the multiple reflection effects within the cavity.**

## Introduction

IN 1984, a series of experiments were carried out at the United Technologies Research Center (UTRC) under the Defense Advanced Research Projects Agency-sponsored Laser Countermeasures Materials Development (LCMMD) program. The tests were conducted to determine the laser hardness of materials designed to resist laser irradiation. Disk targets constructed of different materials were illuminated with a continuous-wave deuterium fluoride laser. Many of these targets were metal-loaded carbons, graphitic materials containing the refractory metals that melt and form a shiny reflecting surface under laser irradiation. This paper describes the techniques developed to simulate these experiments numerically. In these tests, since the laser beam was usually incident on the target at a 45 deg angle, a three-dimensional analysis was required.

Laser ablation is a typical reactive front-moving boundary problem. In this case, however, the transformation is driven by energy supplied from an external source, the laser. The problem has generally been treated using surface-fitting techniques in which the numerical grid is transformed such that the top of the grid corresponds to the ablating surface. For a one-dimensional solution, this can be done straightforwardly using a Landau transformation.[1] In a two-dimensional solution similar transformations have been used.[2] The heat conduction below the surface has generally been solved using finite-difference techniques. The moving finite-element method would also be a useful technique for treating problems of this kind.

In three dimensions, moving grid techniques are more difficult. This is particularly true when simulations are continued until a hole is burned through the target, changing the topology from simply to multiply connected. If three-dimensional simulations are needed, a surface-capturing method with a fixed grid may be more prudent. One obvious way to treat laser ablation in a fixed grid is to model the process as a Stefan problem, that is, to treat it as melting.[3] The enthalpy of ablation is modeled as the heat of fusion of the material. This procedure has been used and it works well, the stored energy in the "ablated" zones contributing to the stability of the thermal conduction modeling. This method was used with a modified version of the HEATING5 code[4] (an explicit three-dimensional heat conduction code with phase-transformation modeling capabilities) as well as with an implicit code that used the Douglas alternating direction implicit (ADI) scheme, generally considered the best of the three-dimensional ADI schemes.[5-7]

The drawback of this method is that it cannot be used to predict the cooldown of a material after the laser has been shut off. In the simulation, the ablated material resolidifies, releasing energy to the target, a clearly unphysical effect. To avoid this problem, later computations were performed with the energy due to ablation within a zone being actually removed, rather than made latent, a variable being used to record the fullness in each zone. A feature of this technique is that as a zone becomes nearly empty, its volumetric heat capacity becomes small and the stability is adversely affected. It thus becomes necessary when a zone is nearly empty to cede the remaining material in a zone of neighboring zone. Fully empty zones have no adverse effect on stability, since they are fully insulating. This numerical model is described more fully in the Appendix.

## Laser-Reflection Analysis

When the laser-beam diameter is comparable to or smaller than the depth of the hole in the target, internal reflection in the crater formed by the laser can become important when modeling shiny materials. To examine the magnitude of the internal reflection effects, the NASA Vehicle Illumination Program (VIP) was used.[8] As shown in Fig. 1, for oblique craters light rays will reflect outward, whereas for acute craters light will focus inward, increasing the peak intensity. As shown in Fig. 2, acute cones will produce a large augmentation in peak intensity. For this reason, ray tracing was included in the modeling. Since ablative recession takes place primarily along the line of laser incidence, it was desirable to use this direction for one of the coordinate axes. Due to the strong anisotropy in the thermal conductivity in many of the materials tested, strict separation in the radial and axial heat conduction was required. (The radial thermal conductivity exceeded the axial conductivity by more than a factor of 100

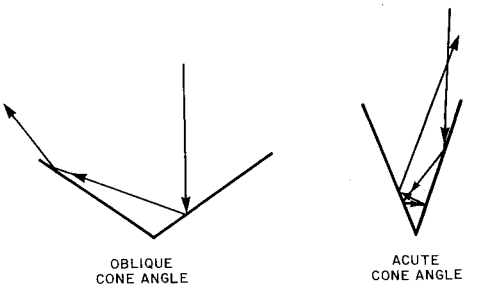


**Fig. 1 Laser reflections for different crater aspect ratios.**

Received June, 1987; revision received Feb. 11, 1988. 

*Principal Scientist.
†Manager, Business Development.

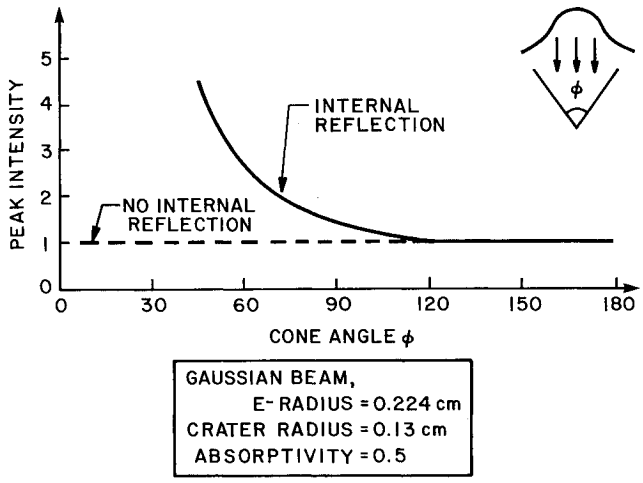


**Fig. 2 Augmentation in intensity due to internal reflections in a crater for a typical Gaussian beam at normal incidence.**

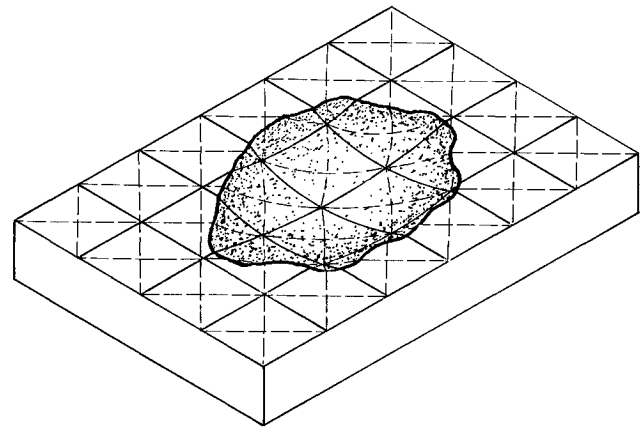

**Fig. 4 Pseudo-three-dimensional view of grid showing triangular reflection facets.**

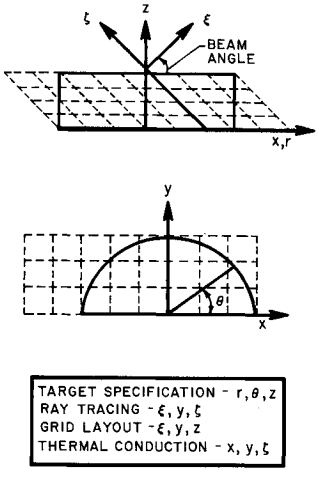


**Fig. 3 Target embedded in nonorthogonal coordinate system.**

in some cases.) This meant that the other two coordinate axes must lie in the natural planes of the material. As shown in Fig. 3, the target was embedded in a nonorthogonal coordinate system ($x$, $y$, $\zeta$), where the $\zeta$ axis is in the laser direction and not necessarily perpendicular to the $x$ axis.

The laser illumination of the target is modeled by launching rays at the target in the $-\zeta$ direction. Rays positions are determined by using a random-number generator weighted to the radial distribution function of the beam, which was Gaussian in the UTRC experiments. That is, if the beam is peaked on the centerline of its axis, then more rays are launched toward the center of disk rather than the edges. An alternative would be to use equal numbers of rays across the disk and weight the importance of the central rays more heavily. The latter technique would be desirable if accurate knowledge of the edge illumination were critical. If, on the other hand, the accuracy of the overall thermal transfer is important (as in this case), then the weighting technique is undesirable. Weighting the central rays heavily would require that many such rays be traced to avoid inaccuracy in the absolute (as opposed to relative) statistical scatter. Making the rays of equal importance this reduces the computational work required.

The crater shape is modeled as a faceted surface. To form this surface, the $\zeta$-direction heights are determined for the center of each pillar defined by the finite-difference mesh. The mesh intersections are then defined as having heights at the center of the four neighboring zones. The surface can then be divided into a set of triangular planes, each defined by three points: a zone center point and two zone intersection points. Thus, each square pillar contains four triangular prisms (Fig. 4). The reason for embedding the cylindrical targets in a rectangular mesh rather than using a cylindrical or transformed mesh is to allow the space through which the rays pass to be subdivided into these triagular prisms. The triangular shapes give an unambiguous definition of the crater surface and its slope, and the flat surfaces provide for computation of the intersection of a ray with the prism boundaries by a simple linear relation. Quadric surfaces would require the solution of a quadratic equation (requiring square roots), and more complex shapes would require an iterative solution.

A ray entering a prism is traced to its intersection with the bottom, top, or one of the sides of the prism. If the ray intersects the bottom of the prism, the ray can be either absorbed or reflected, the result being decided by comparing the surface absorptivity with a random number between zero and one. For specular reflections, a new ray is launched so that its angle equals the angle of incidence of the initial ray with the surface. For diffuse reflection, a cosine-weighted random angle is used. Rather than removing rays striking a surface, their importance could be reduced by the surface absorptivity. If a ray intersects the top of a prism, it is lost and scored as reflected light. A ray intersecting the side of a prism enters a new prism and its progress continues.

After tracing a large number of rays, a distribution of intensity for each pillar is obtained. This distribution will be noisy, since it is obtained using a Monte Carlo process. As the number of rays traced is increased, the noise will decrease, but at a considerable expense of computation time, since the signal-to-noise ratio scales only as the square root of the number of rays traced. To reduce the noise, fits to Legendre polynomials in the $\zeta$ and $y$ directions were sometimes used to smooth the data. This kind of polynomial fit was chosen because it insures that no power is lost or gained in the smoothing operation. This was important, since the amount of ablation is closely related to the power deposited on the target. Use of the smoothing procedure reduced by about a factor of 4 the number of rays that had to be traced for a convergent power profile. The ray-tracing procedure was typically repeated 10–20 times during the simulation to maintain an accurate estimate of the laser power distribution on the target as the crater formed.

Thermal emission from the front surface can also be modeled using the same ray-tracing techniques. Rays are started randomly over the front surface of the disk, their importance determined by the local surface conditions using the Stefan–Boltzmann law

$$\text{Radiation loss} = \text{area } \varepsilon\sigma T^4$$

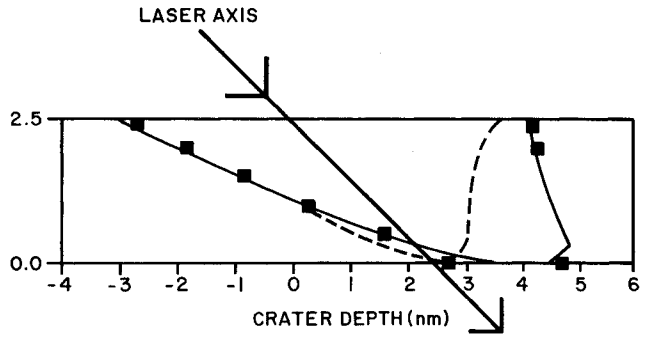


**Fig. 5 Computed final crater profiles of a metal-loaded carbon target with (solid lines) and without (dashed lines) internal reflection compared to post-mortem measurements (boxes).**

where $\varepsilon$ is the emissivity, $T$ the temperature, and $\sigma$ the Stefan-Boltzmann constant. The ray directions are chosen to have a Lambertian cosine distribution. Each of the rays is traced until it is absorbed elsewhere in the crater or is lost. The $T^4$ temperature dependence can be extracted from the net radiation loss from each pillar, leaving only the shape and emissivity factors. The radiation loss can then be recomputed each time step by multiplying this factor by $T^4$. This reduces the need for frequent ray-tracing recomputations to maintain accuracy.

## Results and Conclusions

When numerical simulations on the LCMMD experiments were performed at UTRC, for well-characterized materials it was possible to calculate the time required to burn through the targets, the mass loss, and the crater shapes. Internal reflections in the crater cavities were an important effect, in some cases augmenting peak laser intensity by 100%. An example of the effect of internal reflections on the crater shape of a metal-loaded carbon target is shown in Fig. 5. These materials quickly form a shiny surface under laser ablation. In the experiment, this sample took 1.02 s to burn through and lost 57.0 mg of material. A simulation performed without including the effects of internal reflection produced a burn-through time of 1.27 s and mass loss of 47.1 mg. With the effects of the specular internal reflection included in the simulation, a closer match with a burnthrough time of 1.12 s and mass loss of 59.2 mg resulted, as well as better agreement in crater shape.

Accuracy is required for modeling crater formation, as the process is physically unstable to specular reflections. As seen in Fig. 1, acute craters tend to focus light inward, causing them to become more acute, and oblique craters tend to spread light outward, making them more oblique. Small errors in input parameters or numerical error can result in substantial differences in simulation results.

This study shows that in laser-effects experiments, internal reflections in the crater can significantly affect material performance when using small laser spots on reflective targets. Modelers must use a self-consistent ablation, heat-conduction, and radiation-transport scheme to properly simulate ablation on reflective targets. With a geometrically adquate and consistent formulation, reliable modeling is possible.

## Appendix: Numerical Technique for Ablation and Thermal-Conduction Modeling

In most explicit heat-conduction problems, source rates are computed by linearization, that is, for a source $S$, the new energy $u^{n+1}$ will be

$$\frac{u^{n+1}-u^n}{\Delta t} = S(u^n) + \frac{1}{2}\frac{\mathrm{d}S(u^n)}{\mathrm{d}u}(u^{n+1}-u^n) + \text{conduction terms} \tag{A1}$$

For ablation problems, this technique is inadequate because ablation rates are a very strong function of temperature, a small error in temperature producing a large error in the ablation rate. Ablation rates must be found using an iterative root finder to solve the transcendental equation

$$\frac{u^{n+1}u^n}{\Delta t} = S\left(\frac{u^n+u^{n+1}}{2}\right) + \text{conduction terms} \tag{A2}$$

for $u^{n+1}$. This computation also yields the mass loss to ablation, altering the fullness of the zones.

In the Douglas method[5-7], the heat-diffusion equation

$$\frac{\partial u}{\partial t} = \alpha\left(\frac{\partial^2 u}{\partial x^2}+\frac{\partial^2 u}{\partial y^2}+\frac{\partial^2 u}{\partial z^2}\right) \tag{A3}$$

is solved in three steps. First, an intermediate value $u^*$ is calculated by

$$\frac{u^*-u^n}{\Delta t} = \alpha\frac{\delta^2}{\delta x^2}\left[\frac{1}{2}(u^*+u^n)\right] + \alpha\frac{\delta^2 u^n}{\delta y^2} + \alpha\frac{\delta^2 u^n}{\delta z^2} \tag{A4}$$

where $u^n$ is the value at the old time. In this implicit scheme, for given values of $y$ and $z$, all $x$ values are coupled and solved by a sweep in the $x$ direction of a tridiagonal matrix solver. A second intermediate solution $u^{**}$ is then found by a sweep in the $y$ direction

$$\frac{u^{**}-u^n}{\Delta t} = \alpha\frac{\delta^2}{\delta x^2}\left[\frac{1}{2}(u^*+u^n)\right] + \alpha\frac{\delta^2}{\delta y^2}\left[\frac{1}{2}(u^{**}+u^n)\right] + \alpha\frac{\delta^2 u^n}{\delta z^2} \tag{A5}$$

The final value at the new time $u^{n+1}$ then results from a sweep in the $z$ direction

$$\frac{u^{**}-u^n}{\Delta t} = \alpha\frac{\delta^2}{\delta x^2}\left[\frac{1}{2}(u^*+u^n)\right] + \alpha\frac{\delta^2}{\delta y^2}\left[\frac{1}{2}(u^{**}+u^n)\right] + \alpha\frac{\delta^2}{\delta x^2}\left[\frac{1}{2}(u^{n+1}+u^n)\right] \tag{A6}$$

This method is second-order accurate in space and time and has unconditional linear stability.

The use of a nonorthogonal coordinate system produces an alteration in the form of the Laplacian of the heat-conduction equation

$$\frac{\partial E}{\partial t} = -k\,\nabla^2 T \tag{A7}$$

where

$$\nabla^2 = \frac{\partial^2}{\partial x^2}+\frac{\partial^2}{\partial y^2}+\frac{\partial^2}{\partial z^2} \tag{A8}$$

Now

$$\frac{\partial}{\partial \zeta} = \frac{\partial x}{\partial \zeta}\frac{\partial}{\partial x}+\frac{\partial z}{\partial \zeta}\frac{\partial}{\partial z} \tag{A9}$$

so that

$$\frac{\partial}{\partial z} = \left(\frac{\partial \zeta}{\partial z}\right)\left(\frac{\partial}{\partial \zeta}-\frac{\partial x}{\partial \zeta}\frac{\partial}{\partial x}\right) \tag{A10}$$

$$\frac{\partial^2}{\partial z^2} = \left(\frac{\partial \zeta}{\partial z}\right)^2\left[\frac{\partial^2}{\partial \zeta^2}-2\left(\frac{\partial x}{\partial \zeta}\right)\frac{\partial^2}{\partial x \partial \zeta}+\left(\frac{\partial x}{\partial \zeta}\right)^2\frac{\partial^2}{\partial x^2}\right] \tag{A11}$$

Substituting in Eq. (A8) yields

$$\nabla^2 = \left[1+\left(\frac{\partial \zeta}{\partial z}\right)^2\left(\frac{\partial x}{\partial \zeta}\right)^2\right]\frac{\partial^2}{\partial x^2}+\frac{\partial^2}{\partial y^2}+\left(\frac{\partial \zeta}{\partial z}\right)^2\frac{\partial^2}{\partial \zeta^2} - 2\left(\frac{\partial \zeta}{\partial z}\right)^2\left(\frac{\partial x}{\partial \zeta}\right)\frac{\partial^2}{\partial \zeta \partial x} \tag{A12}$$

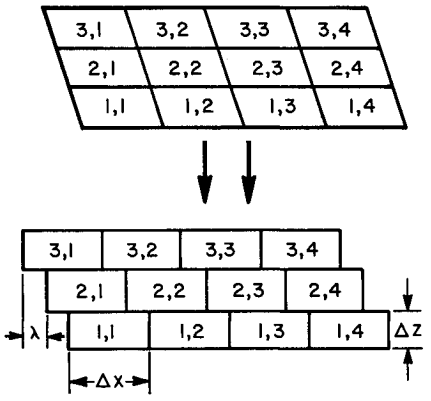


**Fig. 6 Grid zones may be regarded as sloped or staggered.**

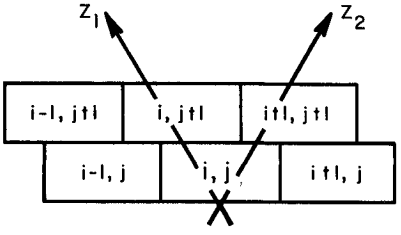


**Fig. 7 Sweep directions of $z_1$ and $z_2$.**

The last term is a mixed derivative with a substantial coefficient for large incidence angles. To handle this term, an additional ADI sweep though the grid is used, as described by Douglas and Gunn.[9] A simpler way of visualizing the problem is to view the mesh as a staggered grid (Fig. 6). The thermal gradient at the top interface of block (1, 1), for example, is

$$\frac{\Delta T}{\Delta z}=\frac{1}{\Delta z}\left[\frac{(\Delta x-\lambda)T_{2,1}+\lambda T_{2,2}}{\Delta x}-T_{1,1}\right]=\left(\frac{\Delta x-\lambda}{\Delta x}\right)\left(\frac{T_{2,1}-T_{1,1}}{\Delta z}\right)+\left(\frac{\lambda}{\Delta x}\right)\left(\frac{T_{2,2}-T_{1,1}}{\Delta z}\right) \tag{A13}$$

The first term here is handled by the $\zeta$-direction sweep and the second term by a crosswise sweep.

The strong anisotropy in the conduction and temperature dependence of the conduction and heat capacity in many of the materials does not permit simple differencing of either the energy or temperature as the variable $u$ given in Eqs. (A3–A6). An accurate and conservative scheme is achieved by computing the differences in the conduction terms rather than their actual values. The solution of the ablation and conduction then becomes a five-step procedure.

Step 1: Solve

$$\frac{E^*-E^n}{\Delta T}=S\left(\frac{E^*-E^n}{2\rho C_p}+T^n\right)-\frac{\delta}{\delta x}\left(k_x\frac{\delta}{\delta x}T^n\right)-\frac{\delta}{\delta y}\left(k_y\frac{\delta}{\delta y}T^n\right)-\left(\frac{\Delta x-\lambda}{\Delta x}\right)\frac{\delta}{\delta z_1}\left(k_z\frac{\delta}{\delta z_1}T^n\right)-\left(\frac{\lambda}{\Delta x}\right)\frac{\delta}{\delta z_2}\left(k_z\frac{\delta}{\delta z_2}T^n\right) \tag{A14}$$

for $E^*$ using a single-variable root finder. The strong nonlinearity of the ablation power loss in the source term makes simple bisection about as efficient as any other technique. Here,

$E^n$ = energy density at the old time
$E^*$ = provisional energy density at the new time
$T^n$ = temperature at the old time
$\Delta t$ = time step
$k_x, k_y, k_z$ = conductivities in the $x$, $y$, and $z$ directions
$\rho$ = material density
$C_p$ = heat capacity

Step 2: Sweep in the $x$ direction to obtain the next estimate of the energy at the new time $E^{**}$

$$\frac{E^{**}-E^n}{\delta t}=S\left(\frac{E^*-E^n}{2\rho C_p}+T^n\right)-\frac{\delta}{\delta x}\left[k\frac{\delta}{\delta x}\left(\frac{E^{**}-E^n}{2\rho C_p}+T^n\right)\right]-\frac{\delta}{\delta y}\left(k_y\frac{\delta}{\delta y}T^n\right)-\left(\frac{\Delta x-\lambda}{\Delta x}\right)\frac{\delta}{\delta z_1}\left(k_z\frac{\delta}{\delta z_1}T^n\right)-\left(\frac{\lambda}{\Delta x}\right)\frac{\delta}{\delta z_2}\left(k_z\frac{\delta}{\delta z_2}T^n\right) \tag{A15}$$

Steps 3, 4, and 5 are similar sweeps in the $y$, $z_1$, and $z_2$ directions, respectively. Here, $\delta/\delta z_1$ is meant to imply the finite difference approximation to the $z$ derivative computed by differences in the values of zones $i$, $k$ and $i$, $k+1$ as shown in Fig. 7. Similarly, $\delta/\delta z_2$ implies the difference approximation using zones $i$, $k$ and $i+1$, $k+1$. The final equation is

$$\frac{E^{n+1}-E^n}{\Delta t}=S\left(\frac{E^*-E^n}{2\rho C_p}+T^n\right)-\frac{\delta}{\delta x}\left[k_x\frac{\delta}{\delta x}\left(\frac{E^{**}-E^n}{2\rho C_p}T^n\right)\right]-\frac{\delta}{\delta y}\left[k_y\frac{\delta}{\delta y}\left(\frac{E^{***}-E^n}{2\rho C_p}\right)+T^n\right]-\left(\frac{\Delta x-\lambda}{\Delta x}\right)\frac{\delta}{\delta z_1}\left[k_z\frac{\delta}{\delta z_1}\left(\frac{E^{****}-E^n}{2\rho C_p}+T^n\right)\right]-\left(\frac{\lambda}{\Delta x}\right)\frac{\delta}{\delta z_2}\left[k_z\frac{\delta}{\delta z_2}\left(\frac{E^{n+1}-E^n}{2\rho C_p}+T^n\right)\right] \tag{A16}$$

where $E^{***}$ and $E^{****}$ are the intermediate values at the new time from the $y$ and $z_1$ sweep, respectively. Accuracy in the values of the heat capacity and conductivity can be achieved by extrapolating forward a half time step or by iteration of the solution process.

## Acknowledgments

The authors would like to thank Leslie Popper, Norman Humer, and Dr. Angeliki Rigos for their help in the construction and use of the laser ablation code. The aid of Dr. Perry Miles and others at Raytheon and BDM in providing and assisting in the interpretation of the experimental data is also appreciated. The authors also wish to thank Dr. Francis W. Patten of the Defense Advance Research Projects Agency for his advice and support during this work.

## References

[1]Landau, H. G., "Heat Conduction in a Melting Solid," *Quarterly of Applied Mathematics*, Vol. 8, 1950, pp. 81–94.

[2]Bonnett, W. S., Ferrell, J. E., and Tang, H., "User Manual—Aerotherm Prediction Procedure for Laser Effects," Aerotherm Rept. UM 75-60, April 1975.

[3]Meyer, G. H., "The Numerical Solution of Multidimensional Stefan Problems," *Moving Boundary Problems*, edited by D. G. Wilson, A. D. Solomon, and P. T. Boggs, Academic Press, New York, 1978, pp. 73–90.

[4]Turner, W. D., Elrod, D. C., and Simantov, I. I., "HEATING5—An IBM 360 Heat Conduction Program," Oak Ridge National Lab., Oak Ridge, TN, Rept. ORNL/CSP/TM-15, 1972.

[5]Douglas, J., "Alternating Direction Implicit Methods for Three Space Variables," *Numerische Mathematik*, Vol. 4, 1962, pp. 41–63.

[6]Roache, P. J., *Computational Fluid Dynamics*, Hermosa Publishers, Albuquerque, NM, 1982, pp. 91–95.

[7]Thibault, J., "Comparison of Nine Three-Dimensional Numerical Methods for the Solution of the Heat Diffusion Equation," *Numerical Heat Transfer*, Vol. 8, 1985, pp. 281–298.

[8]Goldstein, R. and Nagel, R., "Description of the VIP Program for Computing Incident and Absorbed Energy at the Surface of an Orbiting Satellite," NASA Cosmic Program, Athens, GA, GSC-11156, 1969.

[9]Douglas, J. and Gunn, J. E., "A General Formulation of Alternating Direction Methods, Part I. Parabolic and Hyperbolic Problems," *Numerische Mathematik*, Vol. 6, 1964, pp. 428–453.